

## 3D PRINTING

# Imaging-guided deep tissue in vivo sound printing

Elham Davoodi<sup>1</sup>, Jiahong Li<sup>1</sup>, Xiaotian Ma<sup>1</sup>, Alireza Hasani Najafabadi<sup>2</sup>, Jounghyun Yoo<sup>1</sup>, Gengxi Lu<sup>3</sup>, Ehsan Shirzaei Sani<sup>1</sup>, Sunho Lee<sup>1</sup>, Hossein Montazerian<sup>2,4</sup>, Gwangmook Kim<sup>1</sup>, Jason Williams<sup>5</sup>, Jee Won Yang<sup>6</sup>, Yushun Zeng<sup>3</sup>, Lei S. Li<sup>1,7</sup>, Zhiyang Jin<sup>1,6</sup>, Behnam Sadri<sup>1</sup>, Shervin S. Nia<sup>5,8</sup>, Lihong V. Wang<sup>1</sup>, Tzung K. Hsiai<sup>4</sup>, Paul S. Weiss<sup>4,5,8,9</sup>, Qifa Zhou<sup>3</sup>, Ali Khademhosseini<sup>2</sup>, Di Wu<sup>6</sup>, Mikhail G. Shapiro<sup>1,6</sup>, Wei Gao<sup>1\*</sup>

Three-dimensional printing offers promise for patient-specific implants and therapies but is often limited by the need for invasive surgical procedures. To address this, we developed an imaging-guided deep tissue in vivo sound printing (DISP) platform. By incorporating cross-linking agent-loaded low-temperature-sensitive liposomes into bioinks, DISP enables precise, rapid, on-demand cross-linking of diverse functional biomaterials using focused ultrasound. Gas vesicle-based ultrasound imaging provides real-time monitoring and allows for customized pattern creation in live animals. We validated DISP by successfully printing near diseased areas in the mouse bladder and deep within rabbit leg muscles in vivo, demonstrating its potential for localized drug delivery and tissue replacement. DISP's ability to print conductive, drug-loaded, cell-laden, and bioadhesive biomaterials demonstrates its versatility for diverse biomedical applications.

Three-dimensional (3D) bioprinting has emerged as a transformative tool in medicine, enabling the creation of patient-specific implants (1, 2), intricate medical devices (3, 4), and tissue replacements (5–7). Advancing bioink formulations and extrusion- or light-based printing systems (8, 9) have driven this progress, unlocking applications in diverse fields such as tissue regeneration (10, 11), bioelectronics (12, 13), drug delivery (14, 15), and wound sealing (16, 17). However, the implantation of these constructs often requires invasive surgeries, limiting their utility for minimally invasive treatments (18, 19). In vivo printing technologies would enable direct fabrication of bioconstructs at defect sites within the body, eliminating the need for traditional implantation and facilitating rapid, on-site tissue repair. Although near-infrared (NIR) light has been explored as a biosafe energy source for in vivo printing, its applications remain restricted to subcutaneous tissues due to limited light penetration (20, 21).

Ultrasound technology, known for its deep tissue penetration and noninvasive nature, offers a promising platform for in vivo printing. Its real-time imaging capabilities enable precise targeting and control during in situ fabrication of biomaterials (22). Focused ultrasound (FUS), in particular, allows for targeted energy delivery, facilitating processes such as acoustic cavitation induced radical polymerization of materials including polydimethylsiloxane (23, 24) or sonothermally

induced polymerization of poly(ethylene glycol) diacrylate (PEGDA) (25) (table S1).

A major challenge within in vivo printing lies in development of versatile bioink formulations capable of accommodating diverse biomaterials for wide-ranging applicability across various medical scenarios while ensuring high biocompatibility and minimal toxicity from residual prepolymers. Comprehensive in vitro and in vivo studies are essential to address these issues. Additionally, advancing these technologies requires systems capable of large-scale and high-resolution printing, as well as seamless integration with real-time imaging, to ensure precise focal point positioning, minimize off-target tissue effects, and accelerate clinical translation.

We developed an imaging-guided deep tissue in vivo sound printing (DISP) platform, which utilizes low-temperature-sensitive liposomes (LTSLs) as carriers for cross-linking agents to enable precise and controlled in situ fabrication of biomaterials within deep tissues (Fig. 1, A to C, and table S1). In DISP, LTSLs enhance biocompatibility by encapsulating cross-linking agents, preventing premature interaction with surrounding tissues and enabling on-demand release by means of FUS. Designed to respond to mild temperature changes slightly above body temperature, LTSLs enable activation of various cross-linking mechanisms, including ionic, oxidative, and free radical polymerization (Fig. 1, D and E).

DISP achieves high-resolution printing (~150 μm) and fast printing speeds (up to 40 mm s<sup>-1</sup>). A wide range of functional biomaterials, including conductive, drug-loaded, cell-laden, and bioadhesive hydrogels, were successfully printed (Fig. 1, F to H). Gas vesicle (GV)-based ultrasound imaging (26, 27) was integrated into the printing platform, allowing for real-time monitoring of the printing process, precise focal point positioning, and in situ cross-linking verification. As a proof of concept, we demonstrated in vivo printing within the bladders and muscles of live animals, with post procedure analyses confirming the high biocompatibility of both the prepolymers and printed hydrogels.

## The design and mechanism of deep tissue in vivo sound printing

DISP utilizes ultrasound-responsive bioinks—termed US-inks—specifically designed for precise and controlled in situ fabrication. US-inks are composed of biopolymers, cross-linking agent-encapsulated LTSLs, and GVs that act as ultrasound imaging contrast agents. These bioinks are delivered to the target sites through injection or catheters and are located using an ultrasound imaging setup integrated into 3D printing platform. This system accurately targets the FUS focal point onto the US-ink and continuously monitors the printing process.

The FUS transducer, controlled by an automatic positioning system, scans over the US-ink following a predefined G-code. Localized heating induced by FUS triggers the release of cross-linking agent from the LTSLs, enabling immediate in situ cross-linking of the US-ink (Fig. 1, A and B). Transmission electron microscopy (TEM) confirmed the integrity of the LTSLs (Fig. 1C) whereas scanning electron microscopy (SEM) revealed uniform cross-linking and the formation of US-gels (Fig. 1D). DISP enables the synthesis and precise patterning of functional US-gels with diverse properties, including conductivity, biocarrier capacity, and bioadhesion (Fig. 1E), expanding potential applications in bioelectronics, drug delivery, tissue regeneration, wound sealing, and other medical interventions (Fig. 1, F to H).

## Low-temperature-sensitive liposomes for controlled cross-linking

Low-temperature-sensitive liposomes are widely used in drug delivery due to their ability to precisely control release temperatures by engineering lipid bilayer properties. Although certain liposomes can be activated using low-frequency ultrasound from probe sonicators to compromise their membranes for cross-linking applications (28), LTSLs enable remote and precise activation through FUS, allowing superior

<sup>1</sup>Andrew and Peggy Cherng Department of Medical Engineering, Division of Engineering and Applied Science, California Institute of Technology, Pasadena, CA, USA. <sup>2</sup>Terasaki Institute for Biomedical Innovation, Los Angeles, CA, USA. <sup>3</sup>Alfred E. Mann Department of Biomedical Engineering, University of Southern CA, Los Angeles, CA, USA. <sup>4</sup>Department of Bioengineering, University of CA, Los Angeles, Los Angeles, CA, USA. <sup>5</sup>Department of Chemistry and Biochemistry, University of CA, Los Angeles, Los Angeles, CA, USA. <sup>6</sup>Division of Chemistry and Chemical Engineering, CA Institute of Technology, Pasadena, CA, USA. <sup>7</sup>Department of Electrical and Computer Engineering and Department of Bioengineering Rice University, 6100 Main St. Houston, TX, United States. <sup>8</sup>CA Nanosystems Institute, University of California, Los Angeles, Los Angeles, CA, USA. <sup>9</sup>Department of Materials Science and Engineering, University of California, Los Angeles, Los Angeles, CA, USA. \*Corresponding author. Email: weigao@caltech.edu

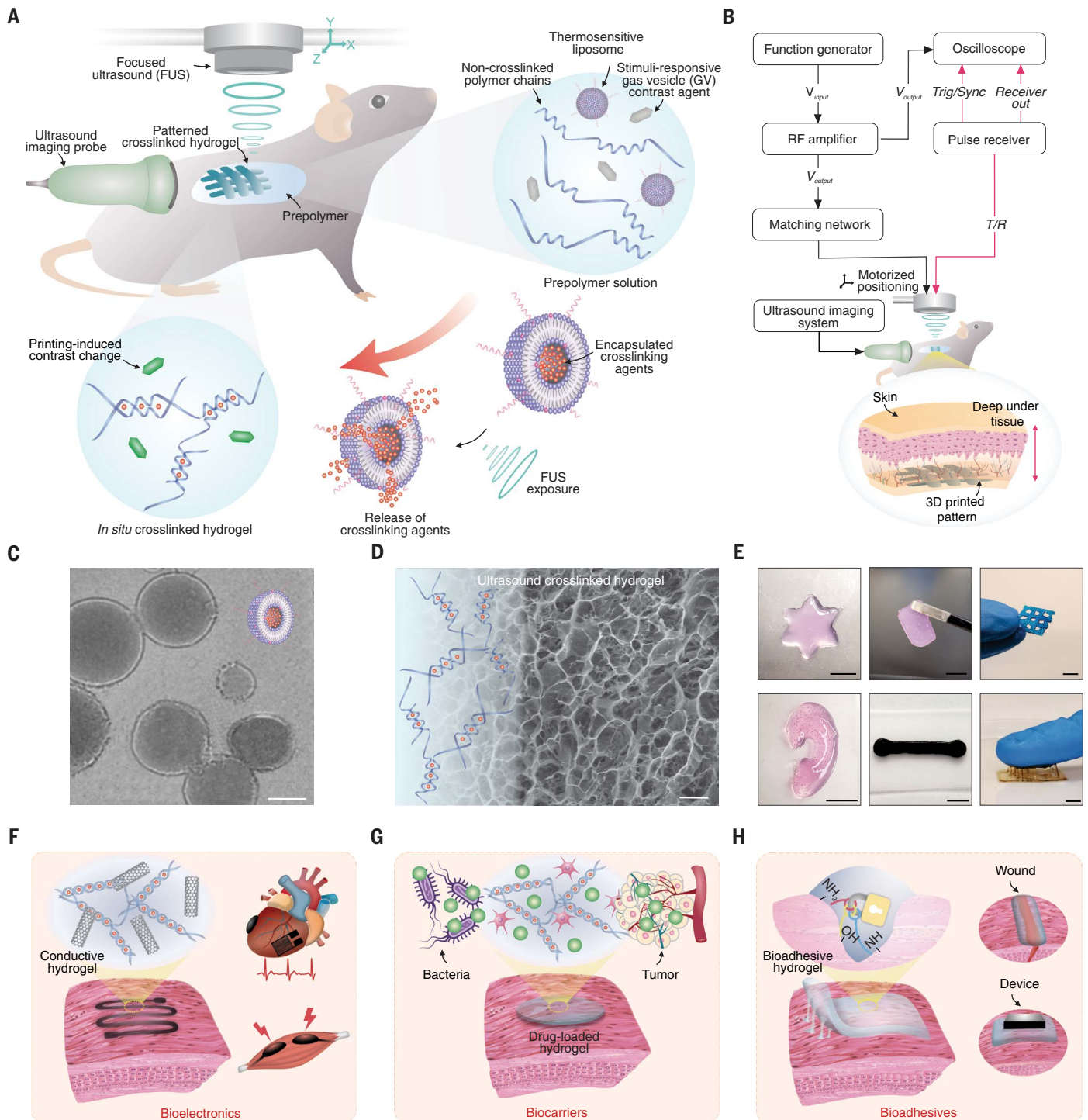


**Fig. 1. Imaging-guided deep tissue in vivo sound printing (DISP).** (A) Schematic of the DISP platform. The DISP system utilizes a US-ink composed of non-cross-linked prepolymer, cross-linking agent-loaded LTSLs, and GVs. The US-ink is injected into the body to noninvasively fabricate a precise functional biostructure in vivo. Integrated GV-based ultrasound imaging is employed to monitor the target organ, detect the presence of the prepolymer, and ensure accurate targeting and successful US-gel formation. (B) In vivo printing setup for FUS generation and monitoring. RF, radio frequency; T/R, transmitter/receiver. (C) TEM image of the cross-linking agent-loaded LTSLs. Scale bar, 100 nm. (D) SEM image of freeze-dried, 3D-printed alginate US-gel. Scale bar, 20  $\mu\text{m}$ . (E) Functional hydrogel structures printed with sound in vivo printing. Scale bars, 5 mm. (F to H) DISP-based in vivo printing of bioelectronic devices for sensing and recording (F), biocarriers for drug delivery and tissue regeneration (G), and bioadhesives for wound sealing and device/tissue interfaces (H).

spatial control. In this study, the LTSLs were designed to remain stable at 37°C and rapidly release encapsulated materials at ~41.7°C (29). Upon FUS exposure, temperature increases locally within the US-ink, which induces a phase transition in the LTSL lipid bilayer from a solid to a liquid state, creating nanopores in the bilayer structure (Fig. 2A).

Grain boundary defects in the solid phase were found to be crucial for the formation of stable nanopores in the lipid bilayers. To enhance lipid mobility and facilitate pore formation, pore-forming lysolipids and a small percentage of PEGylated lipids were incorporated into the lipid bilayer (fig. S1). During heating, these defects expand rapidly

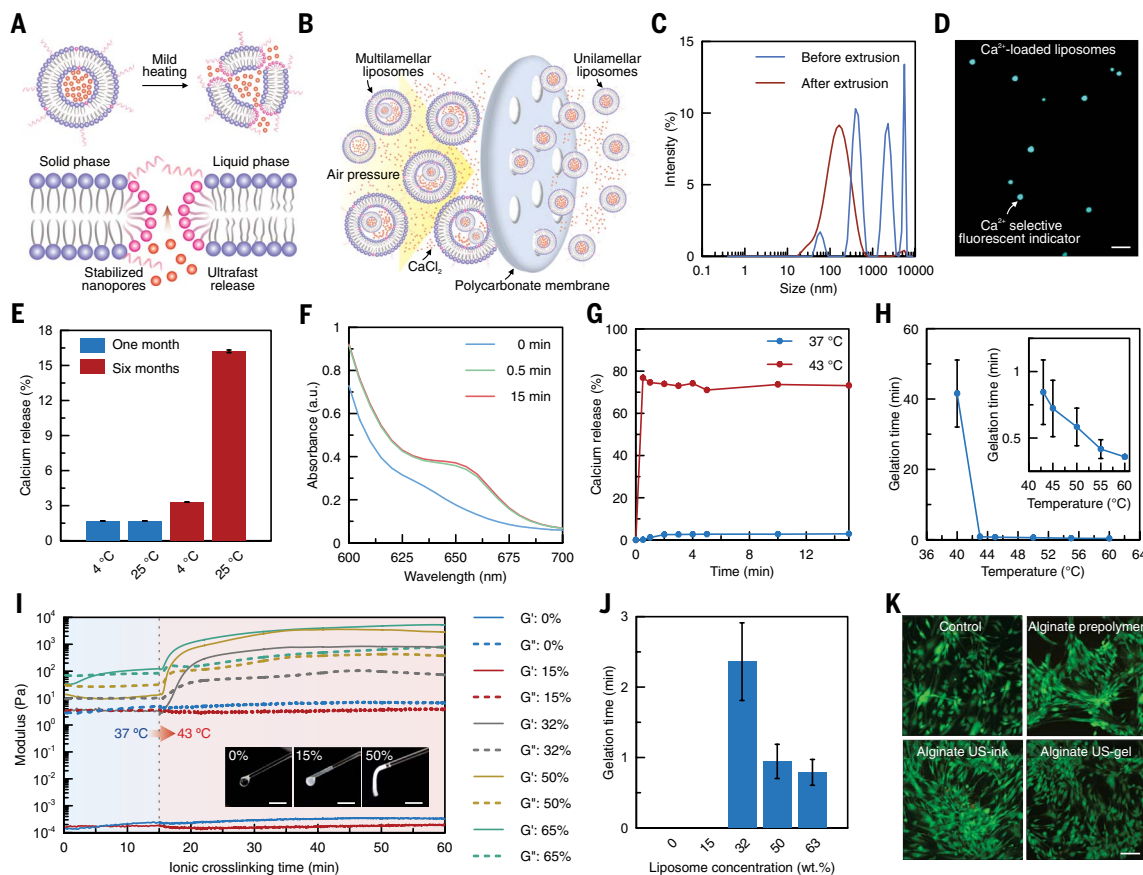


**Fig. 2. Synthesis and characterization of low temperature sensitive liposomes for controlled release of cross-linking agents.** (A) Schematic illustrating the formation of nanoparticles in lipid bilayers of LTSs due to a phase transition from solid to liquid induced by mildly elevated temperatures. (B) Mass production of cross-linking agent (e.g.,  $\text{Ca}^{2+}$ )-loaded LTSs through the extrusion process. (C) DLS analysis of LTSs before and after extrusion. (D) Fluorescent imaging of  $\text{Ca}^{2+}$ -loaded LTSs using fura-2-acetoxymethyl ester as an intracellular calcium indicator. Scale bar,  $3\ \mu\text{m}$ . (E) Stability study showing  $\text{Ca}^{2+}$  release from LTSs stored at  $4^\circ\text{C}$  and  $25^\circ\text{C}$  after 1 month and 6 months. (F) UV-vis analysis of LTSs subjected to  $43^\circ\text{C}$  for various durations. (G) Temperature-dependent  $\text{Ca}^{2+}$  release from LTSs at  $43^\circ\text{C}$  and  $37^\circ\text{C}$ . (H) Cross-linking time for alginate US-inks under various heating temperatures when LTSs concentration is fixed at 50 wt%. (I) Ionic cross-linking of alginate US-inks with varying LTSL concentrations, evaluated by storage ( $G^+$ ) and loss ( $G^-$ ) modulus. (Inset) Images of the gelation status of alginate US-inks containing 0, 15, and 50% LTSs after 30 s of exposure to  $43^\circ\text{C}$ . Scale bars, 5 mm. (J) Cross-linking time measurements for alginate US-inks with different LTSL concentrations. (K) Live/dead staining images of human dermal fibroblast cells cultured for 7 days with the alginate, alginate US-ink containing 50% LTSs, and alginate US-gel. Scale bar,  $100\ \mu\text{m}$ . The error bars in the figures indicate the standard deviation from the mean ( $n = 3$ ).

(29, 30), enabling controlled payload release while minimizing premature leakage at physiological temperatures, ensuring precise and reliable cross-linking for sound printing.

LTSs were synthesized using a dry lipid film hydration process followed by extrusion to achieve uniform size distribution (Fig. 2B and figs. S2 and S3). Dynamic light scattering (DLS) analysis confirmed the successful transition from multilamellar to unilamellar vesicles with smaller and more uniform sizes (Fig. 2C) (29). A zeta potential of  $-17.31\ \text{mV}$  indicated high dispersibility and stability (fig. S3D). Additionally, two-photon microscopy verified the successful encapsulation of a  $\text{CaCl}_2$  cross-linking agent within the LTSs for alginate-based US-inks (Fig. 2D) while unencapsulated  $\text{CaCl}_2$  and other residues were effectively removed through ultracentrifugation (fig. S4).

The LTSs demonstrated long-term stability, maintaining consistent cross-linking performance even after 6 months of storage (Fig. 2E). Ultraviolet-visible (UV-vis) spectroscopy revealed a substantial  $\text{Ca}^{2+}$  release peak at  $650\ \text{nm}$  after 30 s of heating to  $43^\circ\text{C}$  (Fig. 2F). The LTSs showed more than 77% release at  $43^\circ\text{C}$  with negligible release occurring at  $37^\circ\text{C}$ , ensuring controlled, on-demand cross-linking for US-inks (Fig. 2G). Optimizing lipid composition, lysolipid content, and

liposome size can enhance release profiles while balancing permeability and stability to prevent premature leakage, enabling effective cross-linking during sound printing.

Alginate US-ink was prepared by redistributing centrifuged LTSs into an alginate solution. Energy dispersive x-ray spectroscopy (EDS) confirmed the presence of calcium in the alginate US-ink (fig. S5). Elevated temperatures accelerated calcium release and reduced gelation times at fixed LTSL concentrations (Fig. 2H). Rheological studies demonstrated rapid gelation at LTSL concentrations of above 32 weight percent (wt%) (Fig. 2, I and J, and fig. S6A). However, concentrations exceeding 50 wt% led to undesirable self-association within 1 hour at  $37^\circ\text{C}$  (fig. S6, B and C). Therefore, 50 wt% was selected as the optimal concentration for alginate US-inks, enabling on-demand *in situ* alginate cross-linking (fig. S6D) and addressing the limitations of conventional ion diffusion-based cross-linking, which is impractical for *in vivo* applications.

Biocompatibility is critical for both prepolymer and printed structures in biomedical applications. Live/dead viability assays performed on human dermal fibroblasts confirmed high cell viability and normal morphology after 7 days of culture (Fig. 2K and fig. S7).

The US-ink design strategy is versatile, supporting not only ionic cross-linking but also free radical polymerization. As a proof of concept, PEGDA-based US-inks were developed using tetramethylethylenediamine (TEMED)-loaded LTSLs, synthesized and purified in a similar manner (fig. S8A). TEMED release from LTSLs occurred rapidly, within 30 s at 43°C (fig. S8, B and C). These LTSLs were incorporated into a prepolymer mixture containing PEGDA monomers and ammonium persulfate initiator (fig. S9A). At 12% TEMED LTSL concentration, the shortest cross-linking times were achieved at 43°C, with no gelation observed after 1 hour at 37°C (fig. S9, B to E). Importantly, FUS exposure during *in vivo* printing further reduced cross-linking times due to rapid localized heating, outperforming conventional rheological setups.

### FUS-induced high-resolution 3D printing

FUS waves precisely converge on a focal point (Fig. 3A) and effectively penetrate deep into tissues, reaching depths of several centimeters or more, far surpassing other energy delivery methods such as UV, visible, or NIR light, which are limited to a few millimeters as a result of absorption and scattering (Fig. 3B). In the DISP platform, FUS enables high-resolution *in vivo* printing with submillimeter focal zone.

FUS exposure generates localized temperature increases at the focal point through acoustic energy absorption (31). Thermal characterization of the focal point reveals that the heating zone size depends on exposure time and frequency (Fig. 3C), with increased transducer power enhancing both pressure and temperature at the focal point (Fig. 3D and fig. S10, A and B) (32). Pressure zone measurements (Fig. 3,

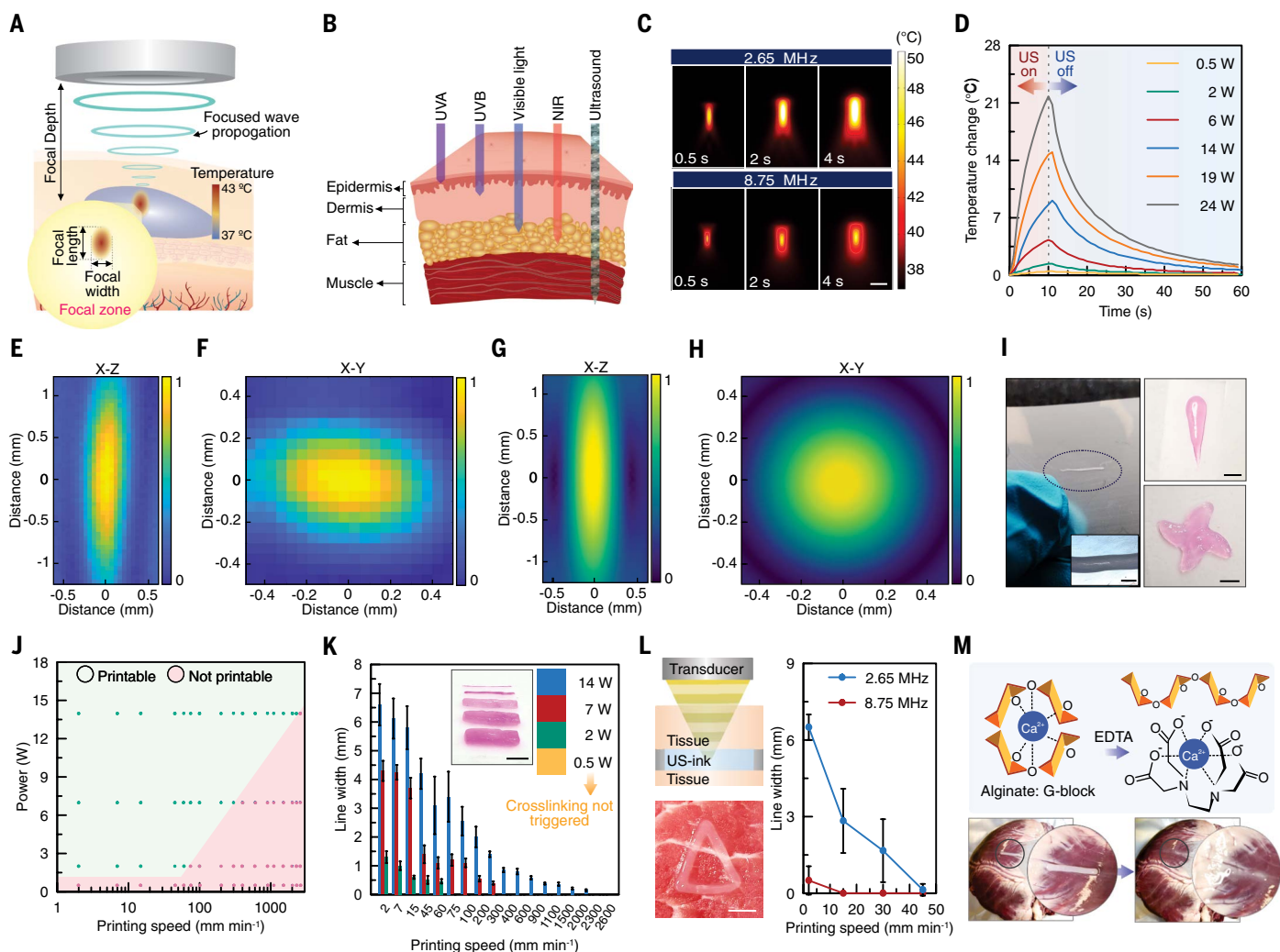


**Fig. 3. Characterization of focused ultrasound-induced 3D printing.** (A) Schematic of FUS wave propagation, illustrating precise targeting of US-ink. (B) Comparison of tissue penetration depths for ultrasound waves versus various light sources, highlighting ultrasound's superior penetration. UVA, ultraviolet A; UVB, ultraviolet B; NIR, near-infrared. Note the inverse relationship between the ultrasound frequency with penetration depth. (C) Thermal simulations showing the temperature distribution at the focal point under different frequencies and exposure times. Scale bar, 2 mm. (D) Temperature profile at the focal point of FUS at 8.75 MHz during and after 10 s of ultrasound exposure. (E to H) Normalized pressure maps at the focal point using a 2.65-MHz transducer, experimental measurements using a hydrophone in the X-Z plane (E) and in the X-Y plane (F), and simulation results in the X-Z plane (G) and in the X-Y plane (H). (I) DISP-printed US-gel patterns. Scale bar for inset, 400  $\mu$ m. Scale bars for patterns on the right, 4 mm. (J) Printability of the alginate US-ink with an 8.75-MHz transducer at various power levels and printing speeds. (K) Printing resolution in terms of line width for alginate US-ink using an 8.75 MHz transducer at different power levels and printing speeds. Scale bar, 5 mm. (L) Printing resolution of alginate US-ink, measured as line width, when printed under 15-mm-thick pork loin tissue at 18 W, with varying frequencies and printing speeds. (Inset) A deep tissue printed pattern on pork tissue. Scale bar, 5 mm. (M) Dissociation of alginate US-gels patterned on tissue using DISP, achieved by 5 min of treatment with 0.025 M EDTA solution. The error bars in the figures indicate the standard deviation from the mean ( $n = 3$ ).

E and F) closely align with simulation results (Fig. 3, G and H and fig. S10, C and D), confirming that focal zone dimensions correlate with transducer frequencies. Simulations further indicate that enlarging transducer aperture reduces the focal zone size, thereby improving precision (fig. S11).

Within US-ink, localized heating and temperature gradients induced by ultrasound absorption trigger LTSL phase changes and initiate cross-linking (fig. S12). The temperature changes remained consistent across multiple FUS exposures (fig. S13). DISP-printed US-gel patterns were optimized by adjusting printing parameters, such as power and speed, at 8.75 MHz (Fig. 3, I to K, figs. S14 to S16, and movie S1), achieving resolutions as fine as 150  $\mu\text{m}$ . Higher frequency FUS with a smaller focal zone and increased printing speed can further enhance resolution. Line width and height characterizations were performed for free-standing printing in a deeper 7-mm US-ink tank (fig. S17). Gradient-sized patterns were produced by varying printing power and speed during the process (fig. S14E).

DISP's capabilities were further demonstrated by printing alginate US-gels beneath ~15 and ~40 mm-thick pork and chicken tissues at various resolutions (Fig. 3L and fig. S18). Additionally, the printed alginate US-gels can be selectively de-cross-linked and removed from tissue using chelate ethylenediaminetetraacetic acid (EDTA) (33) (Fig. 3M and fig. S19).

### Printing of functional biomaterials

The DISP technology offers a versatile platform for printing a wide range of functional biomaterials, unlocking applications in bioelectronics, drug delivery, tissue engineering, wound sealing, and beyond (tables S2 and S3). By enabling precise control over material properties and spatial resolution, DISP is ideal for creating functional structures and patterns directly within living tissues.

Using DISP, we successfully printed hydrogel bioelectronics using alginate US-inks containing conductive additives such as carbon nanotubes (CNTs), Ag nanowires (AgNWs), and MXene flakes (Fig. 4A). DISP's nozzle-free approach avoids clogging issues commonly encountered in traditional printing methods when using inks with high additive concentrations. By optimizing printing parameters—such as speed, power, and CNT concentration—tailored hydrogel circuits with adjustable resistance and patterns were achieved (fig. S20). A calibration curve demonstrated an inverse relationship between resistance and line width, consistent with the theoretical predictions (fig. S20C). Conductive US-inks with CNTs substantially improved both ohmic and ionic conductivity of alginate by nearly an order of magnitude through enhanced electron transfer within CNT networks (fig. S21). Despite increased viscosity due to CNT additives, the ink's shear-thinning properties allowed for effective injection (fig. S22A). CNT-based inks also exhibited shorter gelation times compared with US-inks with other conductive additives (fig. S22, B to D) and slightly wider printed lines than their nonconductive counterparts as a result of higher acoustic absorption (fig. S22E). These conductive US-gels maintained stable conductivity during tensile and compressive loads, making them ideal for wearable and implantable bioelectronics (Fig. 4B and fig. S20, D to F). Additionally, a hybrid ink combining CNTs and AgNWs achieved a tenfold conductivity increase. SEM confirmed the structural integrity and entanglement of CNT fibers within the US-gels (fig. S23). Biocompatibility studies showed no apparent cytotoxicity for conductive US-ink and US-gels (fig. S24). DISP-printed hydrogel bioelectronics demonstrated promising applications for personalized health monitoring, including resistive skin temperature sensors with high sensitivity across physiologically relevant temperature ranges (Fig. 4C) and biopotential electrodes for reliable monitoring of physiological vital signs, such as electrocardiogram (ECG) and electromyogram (EMG) (Fig. 4D).

DISP-printed US-gels can also function as biocarriers, capable of encapsulating a wide range of small and large molecules and thus enabling targeted in vivo printing of therapeutics at the desired

location for sustained and localized drug delivery (Fig. 4, E and F, and figs. S25 to S27). In vitro studies with 3D tumor microspheroids revealed substantially greater cell death after exposure to doxorubicin (Dox)-loaded US-gels compared with the free drug administration. This enhanced therapeutic effect persisted for 3 days, even after multiple media changes, simulating more realistic in vivo conditions (fig. S28).

DISP enables minimally invasive tissue regeneration through in vivo printing of cell-laden hydrogels directly into affected areas. Patterns of cell-laden alginate US-gels were printed at low ultrasound amplitudes, ensuring safe temperature conditions for the cells (fig. S29). The printed cells exhibited high viability for 7 days after printing (Fig. 4, G to I, and fig. S30A), with no substantial cytotoxic effect on morphology or function. Additionally, incorporating cells into the US-ink did not notably alter the prepolymer's rheological properties (fig. S30B). To evaluate the stability of the US-gel, its swelling and degradation in cell media was assessed (fig. S30C). This advance opens new possibilities for minimally invasive tissue regeneration deep within the body.

In vivo printing of bioadhesives offers a noninvasive approach to seal tissue ruptures and lacerations, enabling on-demand formation of bioadhesive patterns over wounds of various shapes. To achieve this, we developed a prepolymer solution of catechol-modified gelatin-catechol acid conjugates (GelCA) (34), with sodium periodate ( $\text{NaIO}_4$ ) encapsulated in the LTSLs to form GelCA US-ink. Upon FUS exposure,  $\text{NaIO}_4$  was released, triggering cross-linking and forming a tissue-adhesive hydrogel (Fig. 4J and fig. S31A).  $\text{NaIO}_4$  was released from LTSLs within 30 s of mild heating at 43°C (fig. S32), producing GelCA US-gel with increased bioadhesion strength (Fig. 4, K and L). The optimal  $\text{NaIO}_4$  LTSL concentration of 20% ensured effective cross-linking without premature gelation after 1 hour at 37°C (fig. S31).

Additionally, the typically nonadhesive alginate US-inks developed adhesive properties when printed using higher US amplitudes and extended exposure times, aligning with literature reports on US-induced adhesion (35). The ultrasound facilitates the integration of the prepolymer into the tissue, followed by in situ cross-linking, which enhances the mechanical interlocking of alginate US-gels within the tissue (Fig. 4, M and N).

### In vivo evaluation of DISP printing in live animals

In vivo experiments were conducted using a mouse model (Fig. 5A and fig. S33). The shear force experienced during the in vivo injection of the prepolymer did not substantially affect the rheological properties of the US-ink (fig. S34A). Additionally, the alginate US-ink stored at 4°C exhibited a long shelf life of at least 450 days, reinforcing its suitability for DISP applications (fig. S34B). As a proof of concept, the DISP technique was used to print US-gels in the mouse bladder, with the goal of developing a potential platform for treating severe bladder cancer.

Ultrasound imaging plays a critical role in precisely positioning the prepolymer within deep tissue, which is vital for effective in vivo applications such as tissue regeneration and drug delivery. Accurate targeting, achieved through meticulous calibration of the FUS transducer relative to the imaging transducer, minimizes the risk of off-target effects and prevents unintended exposure of healthy tissues. Moreover, integrating stimuli-responsive GV contrast agents and GV  $\text{Ca}^{2+}$  sensors with US-ink provides real-time feedback during the printing process (26, 36). This integration confirms US-gel formation, monitors print shape, and tracks cross-linking dynamics. Compared with magnetic resonance imaging-guided techniques used for temperature evaluation at the focal point, GVs offers direct visualization of the printed US-gel (37, 38). Integrating a stimuli-responsive GV contrast agent with prepolymer led to a high contrast allowed for easy visualization of the US-ink using amplitude-modulation (AM) mode ultrasound imaging (27). The inclusion of GVs not only facilitated accurate bioink delivery to the bladder but also enabled confirmation of gel formation

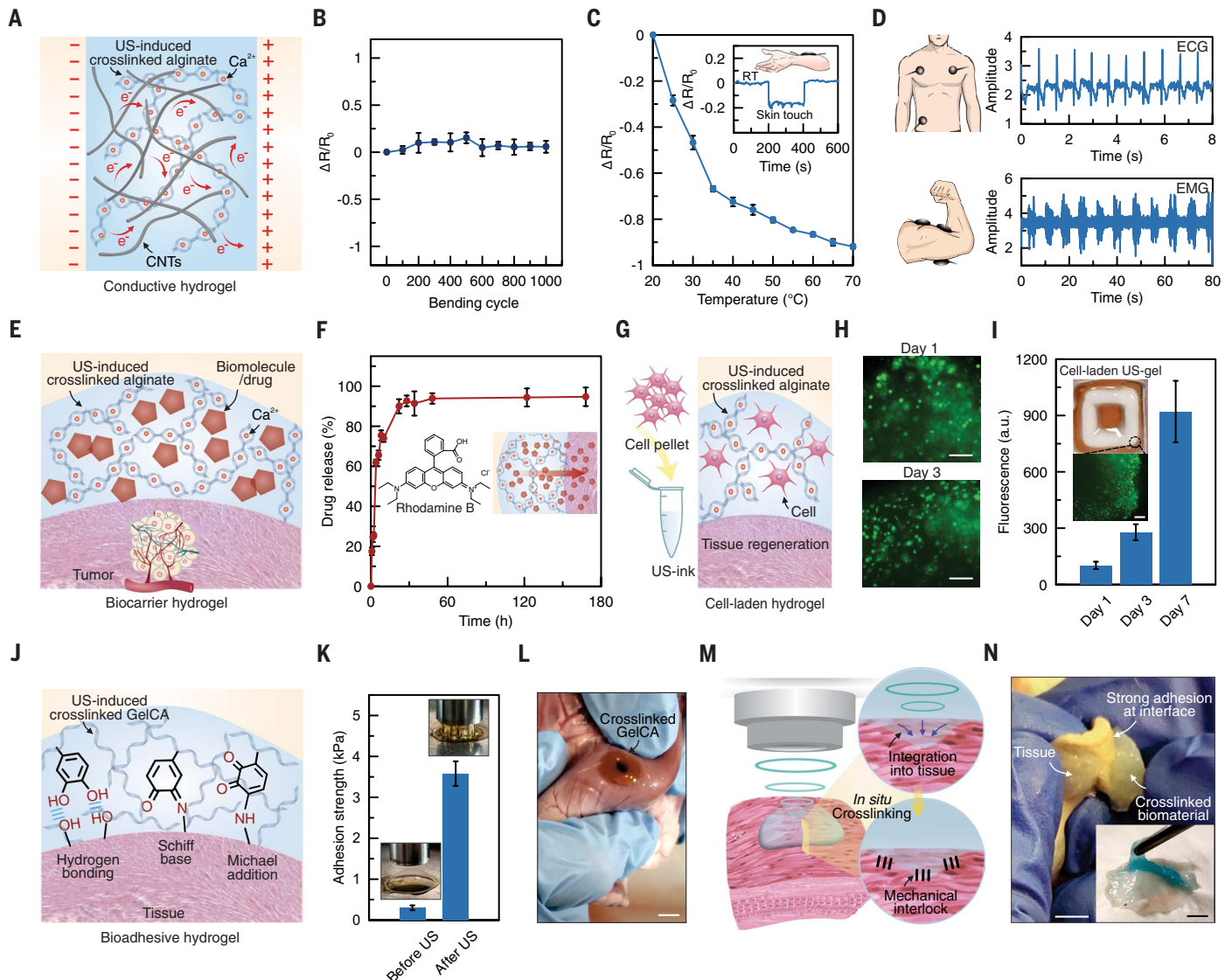


**Fig. 4. Deep tissue in vivo sound printing-based 3D printing of functional biomaterials for various medical applications.** (A) Schematic of conductive US-ink composed of CNT additives entangled within alginate US-ink, cross-linked using FUS. (B) Conductive US-gel patterns maintain stable electrical properties under cyclic bending deformations. (C) Temperature sensing using printed conductive US-gels. (Inset) Consistent and reversible temperature sensor response upon contact with human skin. RT, room temperature. (D) DISP-printed conductive US-gel sensors for ECG and EMG recordings in a human participant. (E) Integration of therapeutic biomolecules within US-ink, forming biocarrier US-gels for potential drug delivery applications. (F) Continuous and sustainable release of a model drug rhodamine B from US-gels. (G) Cell-encapsulated US-gels prepared by integrating cells within biocompatible US-inks followed by printing using an 8.75-MHz transducer at 7 W and a printing speed of 10 mm min<sup>-1</sup>. (H) Live/dead staining images of C2C12 mouse myoblast cells encapsulated within alginate US-gels on days 1 and 3 after printing. Scale bars, 100 μm. (I) Metabolic activity of cells assessed from days 1 to 7 after printing. (Insets) Images of the cell-laden US-gel pattern, printed with an 8.75-MHz transducer at 7 W and 10 mm min<sup>-1</sup>, showing live cells 3 days after printing. Scale bar, 200 μm. (J) Catechol-modified gelatin–caffeic acid conjugates (GelCA) US-inks mixed with NaIO<sub>4</sub> liposomes for bioadhesive applications. (K) Adhesion strength of GelCA US-ink before and after cross-linking. (Inset) Images of the GelCA US-ink before and after mild heating and cross-linking. (L) Ex vivo adhesion testing of GelCA US-gel for sealing punctured heart tissue. Scale bar, 5 mm. (M) In vivo US-induced adhesion, where FUS facilitates prepolymer jetting towards tissue, followed by in situ cross-linking of alginate US-ink to achieve mechanical interlock. (N) Alginate US-gels printed in vivo following intradermal injection of US-ink and cross-linking using a 2.65-MHz transducer at 7 W, with a printing speed of 20 mm min<sup>-1</sup> on live animals. The strong interfacial adhesion is observed between the alginate US-gel and tissue, with blue dye applied for visibility. Scale bars, 6 mm. The error bars in the figures indicate the standard deviation from the mean (*n* = 3).

upon FUS exposure, as the collapse of GV indicated successful targeting (Fig. 5, B and C). This capability enables precise printing directly onto the diseased area of the organ, and the presence of GV in the US-ink had a negligible effect on printing resolution (fig. S33E).

DISP was further explored for localized drug delivery, in which drug-loaded US-gels were printed near the tumor site. Ultrasound imaging was employed to monitor the printing process while the animal was under anesthesia. The catheter's position was monitored using B-mode

ultrasound imaging to ensure successful instillation before injecting the US-ink into the bladder (fig. S35A). FUS was then applied to target the US-ink near the tumor, leading to the collapse of some GV, confirming effective targeting. Clear US-gel was observed from the abdomen of the sacrificed animal, confirming successful in vivo printing (Fig. 5D and fig. S35).

To further assess the Ca<sup>2+</sup> release zone and determine the size and shape of the printed US-gel in situ, GV Ca<sup>2+</sup> sensors were incorporated

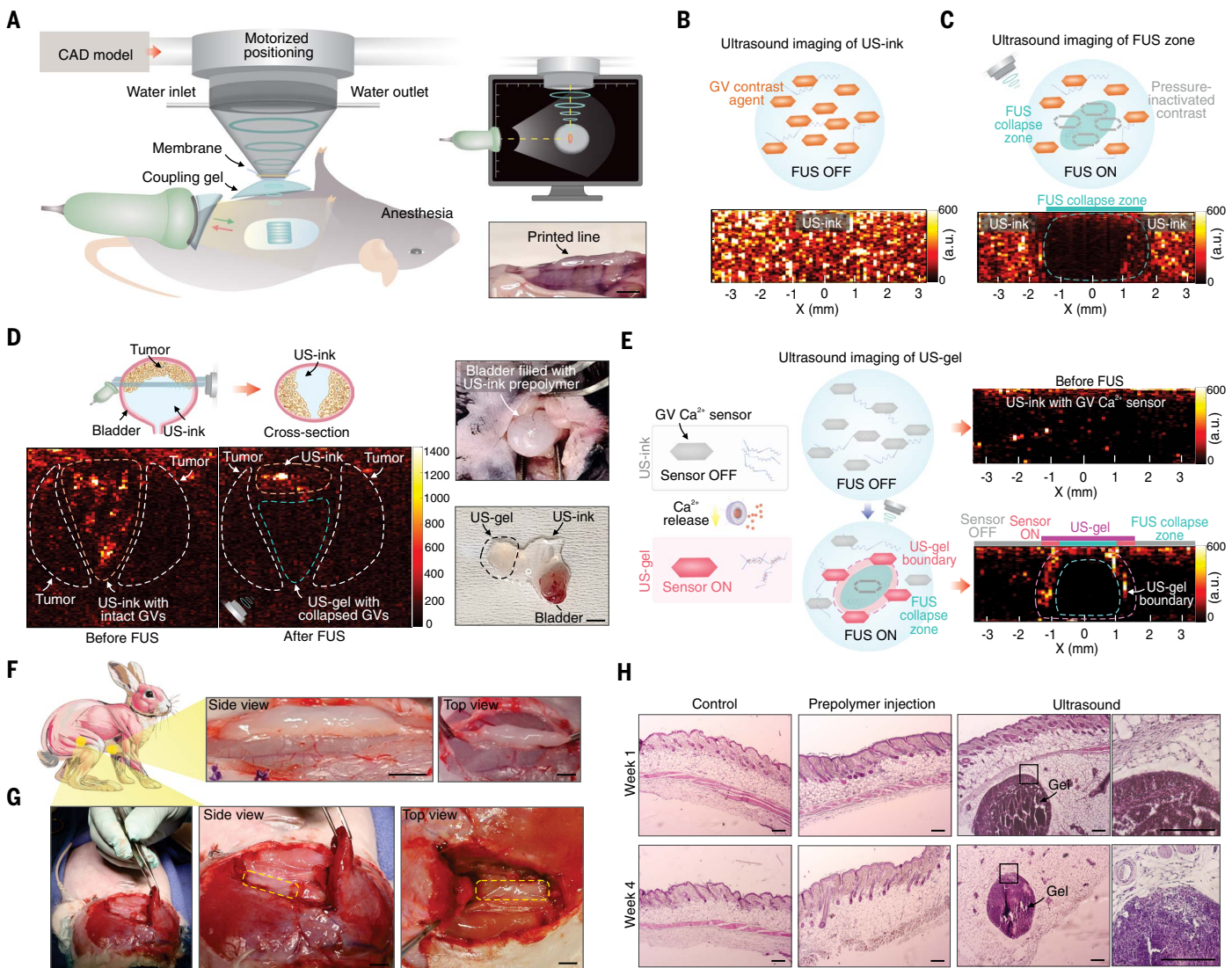


**Fig. 5. Imaging-guided deep tissue sound printing in vivo.** (A) Setup for sound printing in vivo in live animals, employing ultrasound imaging for precise targeting. (Inset) A linear pattern printed in vivo in a mouse. Scale bar, 4 mm. (B and C) Schematic of AM-mode ultrasound imaging with a GV contrast agent used to monitor US-ink distribution in vivo (B) and to ensure precise targeting (C). Ultrasound image inset in (C): A line of GV-integrated alginate US-ink printed and imaged in a cross section. GVs in areas not exposed to FUS remained intact whereas those exposed to FUS collapsed. (D) In vivo printing of US-gels on a tumor site in the bladder of an anesthetized mouse. Successful targeting confirmed by GV collapse. After printing, the mouse bladder was extracted to verify successful printing. Scale bar, 4 mm. (E) In situ  $\text{Ca}^{2+}$  sensing using GV  $\text{Ca}^{2+}$  sensors integrated into alginate US-inks, designed to activate upon exposure to  $\text{Ca}^{2+}$ . A line was printed and imaged in a cross section using AM-mode ultrasound imaging. Higher pressures in the center of the printed line led to partial collapse of GV  $\text{Ca}^{2+}$  sensors whereas GV  $\text{Ca}^{2+}$  sensors at the boundary of the printed US-gel were activated, confirming the shape. (F) US-gel line printed using a 2.65MHz FUS at 11 W and 15 mm  $\text{min}^{-1}$  on the abdominal muscle in a rabbit model. Scale bars, 5 mm. (G) The US-gel line printed deep into the adductor muscle and below the biceps femoris muscle using 2.65 MHz FUS at 20 W and 10 mm  $\text{min}^{-1}$ . Scale bars, 5 mm. (H) In vivo biocompatibility study of US-ink injected intradermally and ultrasound-printed US-gel in mice, assessed through hematoxylin and eosin (H&E) staining of skin tissues at 1 week and 4 weeks after printing. Scale bars, 200  $\mu\text{m}$ .

into the US-ink (39). These sensors remained inactive during AM mode imaging but became activated upon FUS-induced  $\text{Ca}^{2+}$  release, producing noticeable contrast (Fig. 5E and fig. S36). At higher ultrasound amplitudes, some GV  $\text{Ca}^{2+}$  sensors collapsed at the center of the printed structure, where maximum pressure was applied, whereas the boundary of the printed US-gel remained clearly distinguishable.

To demonstrate in larger animal models, both ex vivo and in vivo experiments were conducted on rabbits (Fig. 5, F and G, figs. S37 and S38, and movie S2). Successful in vivo printing was achieved on the exposed abdominal muscle, deep within the adductor muscle, and beneath the biceps femoris muscle, highlighting the ability to target deeper tissue layers for applications such as tissue replacement.

Practical in vivo printing faces challenges such as tissue heterogeneity and dynamic environments that affect ultrasound absorption and cross-linking. Minimal disruption from tissue movement was observed during experiments under anesthesia, but printing on dynamic organs such as the lungs or heart remains challenging. GV  $\text{Ca}^{2+}$  sensors, coupled with AM ultrasound imaging, enable real-time monitoring and adjustment of printing parameters to address these challenges. Future advancements, such as machine learning-based adaptive transducer positioning, could further enhance precision in complex scenarios such as cardiac printing.

In vivo biocompatibility analyses, conducted through hematoxylin and eosin (H&E) and immunofluorescent staining, confirmed

biocompatibility of both the US-ink and resulting US-gel (Fig. 5H and fig. S39). H&E staining showed no tissue damage or abnormal immune cell infiltration whereas immunofluorescent staining revealed minimal proinflammatory activity and macrophage infiltration. CD80 markers showed no significant increase in proinflammatory activity and F4/80 markers indicated macrophage distribution consistent with normal physiological remodeling, without excessive or clustered immune responses. No signs of toxicity were observed, and tissues from other organs showed no notable changes (fig. S40). In the group that received only the US-ink injection, the US-ink was completely cleared by the body in 7 days. However, in the group exposed to FUS, the US-gel persisted (fig. S41).

## Conclusions

Ultrasound-guided in vivo sounder printing using cross-linking agent-loaded LTSLS enables precise, high-speed, high-resolution fabrication of functional biostructures deep within the body. A wide range of bioinks—including conductive, drug-loaded, cell-laden, and bioadhesive formulations—were designed utilizing diverse cross-linking chemistries. Real-time ultrasound imaging ensures precise targeting and controlled in situ cross-linking. Both in vitro and in vivo studies confirmed high biocompatibility of both prepolymers and printed hydrogels. As a proof of concept, in vivo printing was successfully demonstrated in the mouse bladder and rabbit leg muscles, showcasing its potential for targeted therapeutic interventions and tissue replacement.

## REFERENCES AND NOTES

1. S. S. Robinson *et al.*, *Nat. Biomed. Eng.* **2**, 8–16 (2018).
2. I. M. Lei *et al.*, *Nat. Commun.* **12**, 6260 (2021).
3. Y. Bao, N. Paunović, J. Leroux, *Adv. Funct. Mater.* **32**, 2109864 (2022).
4. D. Joung *et al.*, *Adv. Funct. Mater.* **30**, 1906237 (2020).
5. A. C. Weems, M. C. Arno, W. Yu, R. T. R. Huckstepp, A. P. Dove, *Nat. Commun.* **12**, 3771 (2021).
6. Z. Luo *et al.*, *Adv. Funct. Mater.* **34**, 2309173 (2024).
7. Y. Wu *et al.*, *Adv. Funct. Mater.* **34**, 2313088 (2024).
8. N. M. Larson *et al.*, *Nature* **613**, 682–688 (2023).
9. J. T. Toombs *et al.*, *Science* **376**, 308–312 (2022).
10. A. K. Gaharwar, I. Singh, A. Khademhosseini, *Nat. Rev. Mater.* **5**, 686–705 (2020).
11. E. Davoodi *et al.*, *Adv. Healthc. Mater.* **11**, e2102123 (2022).
12. Y. Song *et al.*, *Sci. Adv.* **9**, eadi6492 (2023).
13. T. Zhou *et al.*, *Nat. Mater.* **22**, 895–902 (2023).
14. J. Wang *et al.*, *Adv. Drug Deliv. Rev.* **174**, 294–316 (2021).
15. Q. Ge *et al.*, *Sci. Adv.* **7**, eaba4261 (2021).
16. C. Wang *et al.*, *Nat. Rev. Mater.* **9**, 550–566 (2024).
17. S. J. Wu *et al.*, *Nat. Commun.* **15**, 1215 (2024).
18. Z. Zhu, H. S. Park, M. C. McAlpine, *Sci. Adv.* **6**, eaba5575 (2020).
19. C. Zhou *et al.*, *Nat. Commun.* **12**, 5072 (2021).
20. A. Urciuolo *et al.*, *Nat. Biomed. Eng.* **4**, 901–915 (2020).
21. Y. Chen *et al.*, *Sci. Adv.* **6**, eaba7406 (2020).
22. Y. S. Zhang, A. Dolatshahi-Pirouz, G. Orive, *Science* **385**, 604–606 (2024).

23. M. Habibi, S. Foroughi, V. Karamzadeh, M. Packirisamy, *Nat. Commun.* **13**, 1800 (2022).
24. M. Derayatifar, M. Habibi, R. Bhat, M. Packirisamy, *Nat. Commun.* **15**, 6691 (2024).
25. X. Kuang *et al.*, *Science* **382**, 1148–1155 (2023).
26. M. G. Shapiro *et al.*, *Nat. Nanotechnol.* **9**, 311–316 (2014).
27. D. Maresca, D. P. Sawyer, G. Renaud, A. Lee-Gosselin, M. G. Shapiro, *Phys. Rev. X* **8**, 041002 (2018).
28. V. Nele *et al.*, *Adv. Mater.* **32**, e1905914 (2020).
29. D. Needham, J.-Y. Park, A. M. Wright, J. Tong, *Faraday Discuss.* **161**, 515–534, discussion 563–589 (2013).
30. T. Ta, T. M. Porter, *J. Control. Release* **169**, 112–125 (2013).
31. C. M. I. Quarato *et al.*, *Diagnostics (Basel)* **13**, 855 (2023).
32. R. Cuccaro, C. Magnetto, P. A. G. Albo, A. Troia, S. Lago, *Phys. Procedia* **70**, 187–190 (2015).
33. D. M. Najjar, E. J. Cohen, C. J. Rapuano, P. R. Laibson, *Am. J. Ophthalmol.* **137**, 1056–1064 (2004).
34. H. Montazerian *et al.*, *Cell Rep. Phys. Sci.* **4**, 101259 (2023).
35. Z. Ma *et al.*, *Science* **377**, 751–755 (2022).
36. D. Wu *et al.*, *Sci. Adv.* **9**, eadd9186 (2023).
37. M. de Smet, E. Heijnen, S. Langereis, N. M. Hijnen, H. Grüll, *J. Control. Release* **150**, 102–110 (2011).
38. N. Hijnen *et al.*, *Proc. Natl. Acad. Sci. U.S.A.* **114**, E4802–E4811 (2017).
39. Z. Jin *et al.*, Ultrasonic reporters of calcium for deep tissue imaging of cellular signals. bioRxiv 2023.11.09.566364 [Preprint] (2023); <https://doi.org/10.1101/2023.11.09.566364>

## ACKNOWLEDGMENTS

Fluorescence microscopy was performed at the Advanced Light Microscopy/Spectroscopy Laboratory and Leica Microsystems Center of Excellence at the California NanoSystems Institute at UCLA (RRID:SCR\_022789) with funding support from NIH Shared Instrumentation grant S100D025017 and NSF Major Research Instrumentation grant CHE-0722519. The TEM imaging was supported by the BioPACIFIC Materials Innovation Platform of the National Science Foundation under award DMR-1933487 and by the National Institutes of Health under award S100D18111. **Funding:** This work was funded by the following: National Institutes of Health grants R01DC021461 and R01HL155815 (to W.G.); American Cancer Society grant RSG-21-181-01-CTPS (to W.G.); Heritage Medical Research Institute (to W.G.); National Institutes of Health grant T32EB023858 (to E.D.); National Institutes of Health grant T32GM145388 (to S.S.N.); Challenge Initiative at UCLA (to P.S.W.). **Author contributions:** Conceptualization: E.D. and W.G. Methodology: E.D. and W.G. Investigation: E.D., J.L., X.M., A.H.N., J.Y., G.L., E.S.S., S.L., H.M., G.K., J.W., J.W.Y., Y.Z., L.S.L., Z.J., B.S., S.S.N. Funding acquisition: W.G. Supervision: W.G., L.V.W., T.K.H., P.S.W., Q.Z., A.K., D.W., and M.G.S. Writing - original draft: E.D. and W.G. Writing - review & editing: All authors. **Competing interests:** W.G. is a cofounder and advisor at Prosperity Health. L.S.L. has a financial interest in BLOCH Quantum Imaging Solutions, although the latter did not support this work. W.G. and E.D. are inventors on patent application US18/444,514, submitted by the California Institute of Technology. **Data and materials availability:** The customized finite element analysis code used for thermal simulations of the ultrasound printing process is available upon request. All other data are available in the main text or the supplementary materials. **License information:** Copyright © 2025 the authors, some rights reserved; exclusive licensee American Association for the Advancement of Science. No claim to original US government works. <https://www.science.org/about/science-licenses-journal-article-reuse>

## SUPPLEMENTARY MATERIALS

[science.org/doi/10.1126/science.adt0293](https://science.org/doi/10.1126/science.adt0293)  
Materials and Methods; Figs. S1 to S41; Tables S1 to S3; References (40, 41);  
MDAR Reproducibility Checklist; Movies S1 and S2

Submitted 8 September 2024; accepted 3 March 2025

10.1126/science.adt0293